Photoinduced linkage isomerism of $\{RuNO\}^6$ complexes with bioligands and related chelators†

Anna Zangl,[a] Peter Klüfers,*[a] Dominik Schaniel[b] and Theo Woike*[b]

Received 17th July 2008, Accepted 27th October 2008
First published as an Advance Article on the web 7th January 2009
DOI: 10.1039/b812246f

Five novel complexes containing the $\{RuNO\}^6$ fragment and the anions derived from L-histidine (L-his), *rac*-3-amino-alanine (*rac*-dap), kojic acid (koj), methyliminodiacetic acid (mida), and thiodiacetic acid (tda) have been synthesised and characterised by single-crystal X-ray diffraction analysis, mass spectrometry, spectroscopic methods (NMR, UV–vis, IR) and elemental analysis. In the irradiated complexes, $[Ru(NO)Cl_2(L\text{-his})]$ (**1**), $[Ru(NO)Cl_2(rac\text{-dap})]$ (**2**), $K[Ru(NO)Cl_3(koj)]$ (**3**), $K[Ru(NO)Cl_2(mida)]\cdot\frac{1}{2}H_2O$ (**4**), and $K[Ru(NO)Cl_2(tda)]\cdot H_2O$ (**5**), the existence of the photoinduced long-lived metastable isonitrosyl state S1 and/or the side-on-bonded S2 state were detected by differential scanning calorimetry (DSC) and/or IR spectroscopy. For all complexes **1–5** full geometry optimisation, frequency analysis and calculation of the isotropic magnetic shielding tensors have been conducted in the framework of DFT theory.

Introduction

In the 1980's it was discovered that nitric oxide (NO) plays an important role in a variety of biological processes such as neural signalling, cardiovascular control and cancer reduction.[1–6] Therefore, compounds that act as NO scavengers or release NO, under irradiation for instance, have aroused considerable interest concerning the regulation of NO in the organism. Metal nitrosyl complexes are delivery agents of nitric oxide, which are capable of the photochemical release of NO to biological targets from thermally stable compounds.[7–14] By controlling the irradiation areas and intensities, specific targeting should be possible. Carrier compounds showing controlled release of NO by photodissociation—so called 'caged NO'—are therefore of considerable interest in photodynamic tumour therapy (PDT). Nitrosyl complexes containing a Ru central atom are thermally more stable than Fe nitrosyl complexes. In addition, ruthenium amines, chlorido and polyaminocarboxylate complexes are known to be concentrated by tumour cells.[15] Therefore, biocompatible ruthenium nitrosyl complexes containing these kinds of ligands could be promising targets in PDT.

A further interesting feature of metal nitrosyl complexes is manifest in their ability to form photoinduced long-lived metastable states S1 and S2. Over several decades, the phenomenon of photoinduced linkage isomerism (PLI) of diatomic ligands has been connected with crystalline sodium nitroprusside $Na_2[Fe(CN)_5NO]\cdot 2H_2O$ (SNP).[16] Below −110 °C, the irradiation of SNP with visible light, in the green spectral range, leads to the long-lived metastable states S1 and S2 being located about 1 eV above the ground state (GS). In S1, the NO ligand is existent in a κ*O*-bonded way (isonitrosyl complex) whereas in S2, a side-on coordination in terms of κ*N*,*O* is found.[17] During the last decade it became obvious that PLI is a widespread phenomenon involving—alongside iron nitrosyl complexes—a diversity of ruthenium nitrosyl complexes containing the $\{RuNO\}^6$ fragment.[18–23] $\{RuNO\}^6$ complexes (using the Enemark–Feltham notation[24]) of various, mainly nitrogen, ligands react upon excitation by visible light of lower energy content than necessary for NO photolysis. As with SNP, electronic excitation of the ground state (GS) is followed by relaxation into two metastable NO-linkage isomers: the κ*O*-bonded isonitrosyl S1 state, and the κ*N*,*O* side-on-bonded S2 state (Scheme 1). The light-induced species are metastable with practically infinite lifetimes when kept below their specific decay temperature (T_d), which can be determined by differential scanning calorimetry (DSC) and temperature-dependent IR experiments.[20] Owing to the unprecedented large differences in the refractivity indices of the various photoinduced isomers, holographic data storage is a technically attractive issue of PLI research.[25–28] The various photosensitive ruthenium nitrosyl complexes present a wide range of decay temperatures. For information storage systems, the linkage isomers are required to be stable at room temperature. Therefore, a continuous search for novel ruthenium nitrosyl compounds is in progress.

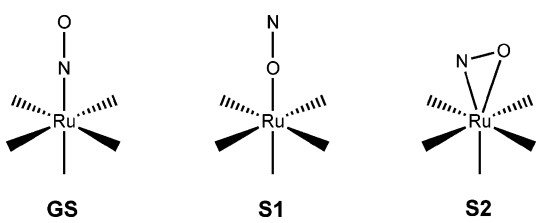

Scheme 1 Schematic illustration of the GS, S1 and S2 binding mode in $\{RuNO\}^6$ complexes.

[a]*Department für Chemie und Biochemie der Ludwig-Maximilians-Universität, Butenandtstraße 5–13, 81377 München, Germany. E-mail: kluef@cup.uni-muenchen.de; Fax: +49 89 2180 77407*
[b]*Physikalisches Institut der Universität zu Köln, Zülpicher Straße 77, 50937 Köln, Germany. E-mail: th.woike@uni-koeln.de*

† Electronic supplementary information (ESI) available: Rotatable 3-D crystal structure diagrams. CCDC reference numbers 685117 (**1**), 685118 (**2**), 685119 (**3**), 685120 (**4**) and 685121 (**5**). For ESI and crystallographic data in CIF or other electronic format see DOI: 10.1039/b812246f

Since PLI is a distinctly stepwise process compared to photorelease of NO, PLI-directed work will contribute to an understanding and control of the basic steps of reactions that are connected to NO chemistry and biochemistry including physiological NO release, NO metabolism at metal centers and NO-related technical catalysis. The latter points draw one's attention to the details of the PLI mechanism, the first step of which is the weakening of metal-to-NO back bonding by the population of the NO-π* orbital in the electronically excited state—a process that may also occur in the dark *via* electron transfer by a reductant.

Laying the focus on the ligand decoration of a single complex molecule or ion, we can recognize some unclearly developed dependencies, among them not only properties of the *trans*- but also of the *cis*-to-NO-bonded ligands. The life span and the population of metastable states thus appear to increase if the *cis* ligands do not exhibit π effects. Hence, salts of the $[Ru(NO)(NH_3)_5]^{3+}$ ion show maximum population and decay temperatures, whereas the much lower reachable populations of metastable states of the related $[Ru(NO)Cl_5]^{2-}$ anion structurally relax at much lower temperatures.[22,23,29,30] Intermediate critical parameters were found for *trans*-$[Ru(NO)(NH_3)_4Cl]^{2+}$, thus underlining that it is not only the *trans*-bonded ligand, which determines the PLI characteristics of a species.[31] Maximum values for the population of the structurally excited states have recently been reported for another *trans*-chlorido complex, the fluoridoborate hemihydrate of the *trans*-$[Ru(NO)(py)_4Cl]^{2+}$ ion (py = pyridine).[32] As in the amine complex, no notable π contributions have to be assigned to the ruthenium–pyridine bonds due to the lack of coplanarity of the aromatic rings and the complex's equatorial plane.

Since there are already a few studies in which the *trans* effect in {RuNO}^{6} complexes has been investigated,[18,20,23,33,34] we opted for a different approach by retaining the *trans* ligand/atom and varying the *cis* ligands/atoms instead. To shed light on structure–stability dependencies, we have prepared new {RuNO}^{6} complexes that combine, among others, the (virtually beneficial) amine *cis* ligation and the (virtually detrimental) chlorido *cis* ligation. The amino acid L-histidine, the hydroxypyrone kojic acid, the amino acid derivative *rac*-3-amino-alanine and the dicarboxylic acids methyliminodiacetic acid and thiodiglycolic acid exhibit a high affinity toward the {RuNO}^{6} fragment providing a number of hitherto unknown bioinorganic complexes with the common feature of an oxygen atom *trans* to NO. Although biomolecules have been used as ligands for the {RuNO}^{6} center in medically motivated studies,[15,35] they have not as yet been in the focus of PLI research. In order to contribute to an integrated view to nitrosyl excitation, the focus of this article is the detection of the PLI phenomenon of {RuNO}^{6} complexes of some typical bioligands and derivatives thereof.

Results and discussion

The biomolecules L-histidine, *rac*-2,3-diaminopropionic acid (*rac*-3-amino-alanine), and kojic acid, as well as the related dicarboxylic acids methyliminodiacetic acid and thiodiacetic acid (Scheme 2) were coordinated to a {RuNO}^{6} fragment as a monoanion (A–C) or a dianion (D, E). The ligands A–E in their deprotonated state are denoted as L-his, *rac*-dap, koj, mida and tda, respectively. With the exception of the bidentate koj, the other ligands (L^{n-}) bind in a tridentate mode according to the general reaction scheme:

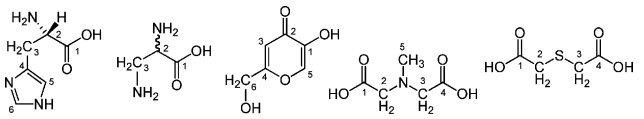

Scheme 2 The parent acids of the ligands used in this work including atom numbering for the NMR part: L-histidine (A), *rac*-3-amino-alanine (B), kojic acid (C), methyliminodiacetic acid (D) and thiodiacetic acid (E).

$$[Ru^{III}(NO)Cl_5]^{2-} + L^{n-} \rightarrow [Ru^{III}(NO)(L)Cl_2]^{1-n} + 3Cl^-$$

In each case, the remaining coordination sites in the resulting octahedral complexes are occupied by chlorido ligands (Scheme 3). Accordingly, the formulae of the new compounds are $[Ru(NO)Cl_2$(L-his)] (**1**) and $[Ru(NO)Cl_2$(*rac*-dap)] (**2**) for two electroneutral complexes, which are soluble in DMSO and, partially, in DMF, whereas the anionic complexes were isolated as $K[Ru(NO)Cl_3$(koj)] (**3**), $K[Ru(NO)Cl_2$(mida)]$\cdot\frac{1}{2}H_2O$ (**4**) and $K[Ru(NO)Cl_2$(tda)]$\cdot H_2O$ (**5**). The salts dissolved readily in water and were recrystallized from the aqueous solutions. Structural analyses on the light- to dark-orange crystals were obtained for all compounds (Fig. 1–5).

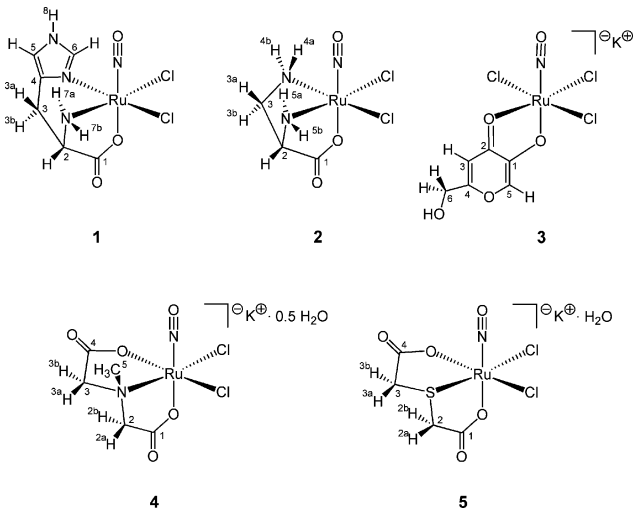

Scheme 3 An overview of the novel complexes with the atom numbering used in the NMR section: $[Ru(NO)Cl_2$(L-his)] (**1**), $[Ru(NO)Cl_2$(*rac*-dap)] (**2**), $K[Ru(NO)Cl_3$(koj)] (**3**), $K[Ru(NO)Cl_2$(mida)]$\cdot\frac{1}{2}H_2O$ (**4**) and $K[Ru(NO)Cl_2$(tda)]$\cdot H_2O$ (**5**).

X-Ray structures

Structural information on {RuNO}^{6} complexes with the ligands of this work is sparse. To the best of our knowledge, the only crystal structure analysis has been published by Efimenko *et al.*,[35] who investigated the crystal structure of $(NH_4)[Ru(NO)(tdaH)Cl_3]$. Thiodiacetic acid is coordinated as a monoanionic, bidentate ligand, which binds equatorially through the sulfur donor and one carboxylate-O atom *trans* to NO. The second carboxylate group of tda is pendant and protonated, obviously due to the acidic mother liquor.

Literature about related complexes of L-histidine[35]and methyliminodiacetic acid[35] with the {RuNO}^{6} fragment use spectrometric data on reaction mixtures for structural assignment.

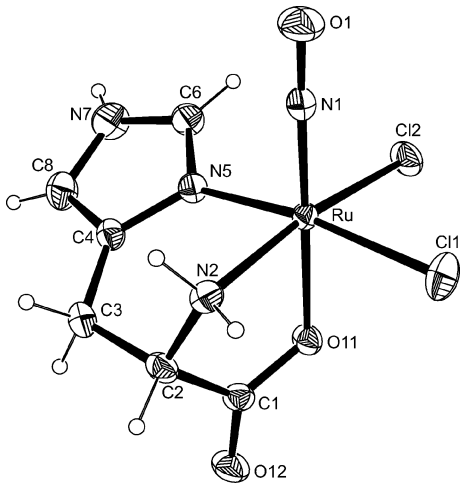

Fig. 1 Structure of [Ru(NO)Cl_2(L-his)] (**1**) (50% probability ellipsoids). Interatomic distances [Å] and angles [°] (with standard deviations in parentheses): Ru–N1 1.726(2), Ru–Cl1 2.3653(7), Ru–Cl2 2.3702(7), Ru–O11 2.0102 (19), Ru–N2 2.075(2), Ru–N5 2.072(2), N1–O1 1.149(3); Cl1–Ru–N1 92.95(8), Cl2–Ru–N1 92.37(8), O11–Ru–N1 178.66(10), O11–Ru–N2 79.92(8), O11–Ru–N5 85.32(8), N1–Ru–N2 98.73(11), N1–Ru–N5 94.63(10), N2–Ru–N5 86.53(10), Ru–N1–O1 177.7(2); puckering analysis: Ru–O11–C1–C2–N2: Q_2 = 0.397(2) Å, φ_2 = 149.5(4)°, Ru–N2–C2–C3–C4–N5: Q = 0.685(3) Å, φ = 129.9(3)°, τ = 252.1(3)°; donor–acceptor distances in hydrogen bonds: N2 ··· Cl2^{i} 3.359(2), N2 ··· Cl1^{i} 3.567(3), N2 ··· O12^{ii} 2.857(3), N7 ··· O12^{iii} 2.985(4), N7 ··· Cl2^{iv} 3.393(3). Symmetry codes: ^{i} $-x+2, y-\frac{1}{2}, -z+\frac{1}{2}$; ^{ii} $x+\frac{1}{2}, -y+\frac{1}{2}, -z$; ^{iii} $-x+1, y-\frac{1}{2}, -z+\frac{1}{2}$; ^{iv} $x-\frac{1}{2}, -y+\frac{1}{2}, -z+1$.

Slocik *et al.* studied the interaction of L-histidine and methyliminodiacetic acid with the 'caged NO' reagent [Ru(NO)$Cl_3(H_2O)_2$] by using NMR/IR methods (L-histidine, methyliminodiacetic acid) and ESI-MS (methyliminodiacetic acid).[36] As to the complexation of L-histidine to the {RuNO}^{6} fragment, they assumed the formation of two isomers: in a major species [Ru(NO)$Cl_3(H_2O)$(L-his)]$^-$ (75%), L-histidine is supposed to coordinate *trans* to NO in a monodentate fashion *via* the imidazole ring, whereas the amino group is H-bonded to an aqua or chlorido ligand of the equatorial set and the carboxylate group remains pendant. In a minor species [Ru(NO)Cl_3(L-his)]$^-$ (25%), the equatorial aqua ligand is displaced by the amino group, which leads to a bidentate chelate complex. As to the complexation of methyliminodiacetic acid to {RuNO}^{6}, Slocik *et al.* found a mixture of three neutral isomers [Ru(NO)Cl(H_2O)(mida)], each mida obviously coordinating in a tridentate fashion. The main species (85%) has one glycinato group chelated equatorially with the central amine donor, the other glycinato donor is coordinated axially. In the two minor species, the amine donor is located *trans* to NO and the two glycinato groups in the equatorial plane coordinate either *cis* (9%) or *trans* (6%) to each other.

Borges *et al.*[37] synthesised the distantly related {RuNO}^{6} complex [Ru(NO)$(NH_3)_4$(L-hisH)]$(BF_4)_3$, in which L-histidine coordinates *trans* to NO in a monodentate mode *via* an imidazole-N atom. The compound was characterised by elemental analysis, molar conductance measurements, UV-vis, IR and ^{1}H NMR spectroscopy, and electrochemical techniques. Balakaeva *et al.*[38] investigated the reaction of L-methionine with the {RuNO}^{6} fragment and succeeded in obtaining the crystal structure of complex [Ru(NO)Cl_2(met)], which is quite similar to [Ru(NO)Cl_2(L-his)] (**1**). Both amino acids coordinate in a tridentate mode with the carboxylate group *trans* to NO.

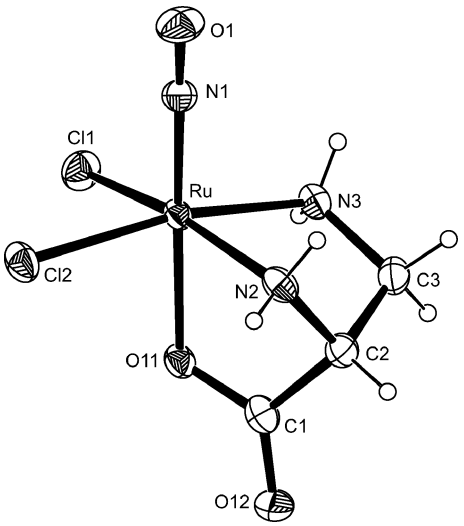

Fig. 2 Structure of [Ru(NO)Cl_2(*rac*-dap)] (**2**) (50% probability ellipsoids). Interatomic distances [Å] and angles [°] (with standard deviations in parentheses): Ru–N1 1.735(3), Ru–O11 2.019(2), Ru–N2 2.081(3), Ru–N3 2.088(3), Ru–Cl1 2.3632(8), Ru–Cl2 2.3813(9), N1–O1 1.146(3); Cl1–Ru–N1 100.25(9), Cl2–Ru–N1 91.12(10), O11–Ru–N1 172.29(11), O11–Ru–N2 78.84(10), O11–Ru–N3 83.10(10), N1–Ru–N2 94.39(12), N1–Ru–N3 99.50(12), N2–Ru–N3 80.31(12), Ru–N1–O1 171.0(3); puckering analysis: Ru–O11–C1–C2–N2: Q_2 = 0.579(3) Å, φ_2 = 324.1(3)°, Ru–N2–C2–C3–N3: Q_2 = 0.612(3) Å, φ_2 = 41.5(3)°, Ru–O11–C1–C2–C3–N3: Q = 1.145(3) Å, φ = 99.41(15)°, τ = 176.75(16)°; donor–acceptor distances in hydrogen bonds: N2 ··· Cl1^{i} 3.202(3), N2 ··· O11^{ii} 3.259(4), N2 ··· Cl1^{ii} 3.491(3), N2 ··· Cl2^{ii} 3.601(3), N3 ··· O12^{ii} 2.935(4), N3 ··· O11^{ii} 3.068(4), N3 ··· Cl2^{iii} 3.307(3). Symmetry codes: ^{i} $-x+2, y+\frac{1}{2}, -z+\frac{1}{2}$; ^{ii} $x, -y+\frac{1}{2}, z+\frac{1}{2}$; ^{iii} $x-1, y, z$.

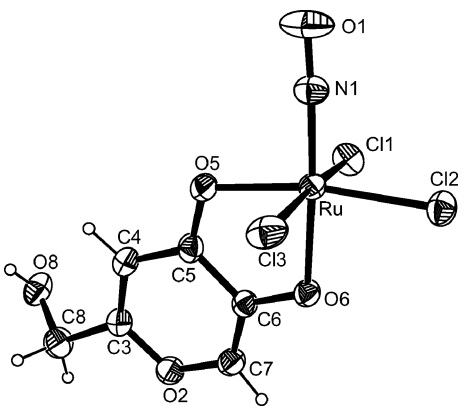

Fig. 3 Structure of K[Ru(NO)Cl_3(koj)] (**3**) (50% probability ellipsoids, potassium counterion not depicted). Interatomic distances [Å] and angles [°] (with standard deviations in parentheses): Ru–N1 1.732(3), Ru–Cl1 2.3635(8), Ru–Cl2 2.3498(8), Ru–Cl3 2.3768(8), Ru–O5 2.060(2), Ru–O6 2.0174(19), N1–O1 1.146(3); Cl1–Ru–N1 92.40(9), Cl2–Ru–N1 95.39(9), Cl3–Ru–N1 93.67(9), O5–Ru–O6 81.57(8), O5–Ru–N1 94.62(10), O6–Ru–N1 175.87(11), Ru–N1–O1 175.7(3). Puckering analysis: Ru–O5–C5–C6–O6: Q_2 = 0.098(2) Å, φ_2 = 344.8(17)°; donor–acceptor distance in hydrogen bond: O8 ··· Cl3^{i} 3.129(3). Symmetry code: ^{i} $-x, -y+1, -z+1$.

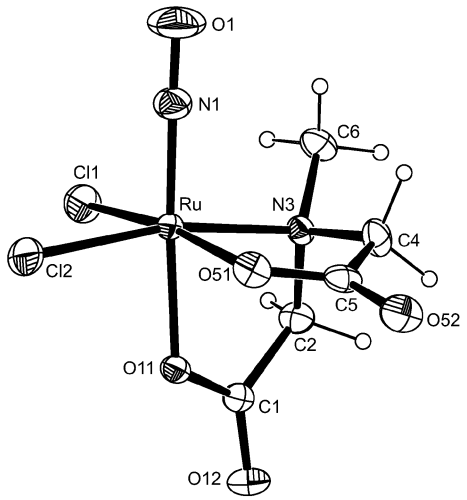

Fig. 4 Structure of K[Ru(NO)Cl_2(mida)]·$\frac{1}{2}H_2O$ (**4**) (50% probability ellipsoids, crystal water and potassium counterion not depicted). Interatomic distances [Å] and angles [°] (with standard deviations in parentheses): Ru–N1 1.7399(18), Ru–N3 2.0943(15), Ru–O51 2.0561(14), Ru–O11 2.0252(13), Ru–Cl1 2.3371(5), Ru–Cl2 2.3613(5), N1–O1 1.138(2); Cl1–Ru–N1 92.34(7), Cl2–Ru–N1 95.55(6), O11–Ru–N1 176.46(7), O11–Ru–N3 80.97(6), O51–Ru–N1 97.08(8), O51–Ru–N3 83.93(6), N1–Ru–N3 95.75(7), Ru–N1–O1 176.55(18). Puckering analysis: Ru–O11–C1–C2–N3: Q_2 = 0.3302(15) Å, φ_2 = 324.8(3)°, Ru–O51-C5-C4-N3: Q_2 = 0.2161(18) Å, φ_2 = 121.3(4)°; no hydrogen bonds detected.

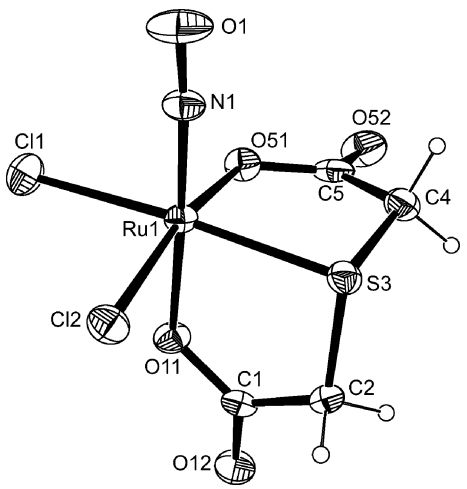

Fig. 5 Structure of K[Ru(NO)Cl_2(tda)]·H_2O (**5**) (50% probability ellipsoids, crystal water and potassium counterion omitted, only one of two ruthenate ions of the asymmetric unit depicted). Interatomic distances [Å] and angles [°] (with standard deviations in parentheses): Ru1–N1 1.741(3), Ru1–Cl1 2.3799(9), Ru1–Cl2 2.3797(9), Ru1–S3 2.3232(9), Ru1–O11 2.013(2), Ru1–O51 2.030(2), N1–O1 1.142(4); Cl1–Ru1–N1 90.93(11), Cl2–Ru1–N1 92.35(11), S3–Ru1–N1 96.75(11), O11–Ru1–O51 82.33(10), O11–Ru1–N1 177.59(13), O51–Ru1–N1 98.09(12), Ru1–N1–O1 176.1(3). Puckering analysis: Ru1–S3–C2–C1–O11: Q_2 = 0.202(3) Å, φ_2 = 44.5(9)°, Ru1–S3–C4–C5–O51: Q_2 = 0.226(3) Å, φ_2 = 228.8(7)°; donor–acceptor distances in hydrogen bonds: O91 ··· O12 2.913(5), O91 ··· O51^{i} 2.952(4), O92 ··· O52^{ii} 3.068(5), O92 ··· O51^{ii} 3.219(5). Symmetry codes: ^{i} x, $y-1$, z; ^{ii} $x-1$, y, z.

The molecular structures in crystals of **1–5** are depicted in Fig. 1–5, together with the most significant bond distances and angles, a puckering analysis,[39] and hydrogen bonds. Crystallographic data are listed in Table 1.

Crystals of **1** and **2** consist of neutral [Ru(NO)Cl_2(L-his)] and [Ru(NO)Cl_2(dap)] molecules, respectively. Both compounds are devoid of solvent molecules in their unit cells. The ruthenium centres are in a distorted octahedral environment with the nitrosyl and the carboxylate groups defining the molecular axis. The equatorial plane contains two *cis*-chlorido ligands and two *cis*-nitrogen atoms in each case. The ligands L-his and dap coordinate facially tridentate—compare the mono and bidentate binding modes that have been derived by Slocik *et al.* from the spectrometric analysis.[35] Analogously, the ruthenate ions in **3**, **4** and **5** possess a distorted octahedral structure with the axial positions occupied by nitrosyl groups and oxygen atoms. The equatorial plane is occupied by three chlorido ligands and one carboxylato-oxygen atom (**3**), two chlorido ligands, one nitrogen and one oxygen atom (**4**), or two chlorido ligands together with one nitrogen and one sulfur atom (**5**). As with L-his and dap, the ligands mida and tda are facially coordinated.

The crystal structures of **3–5** show a normal bonding situation of the counterions, which are coordinated by 7–8 chlorine or oxygen next neighbours. The structures of **1**, **2** and **5** exhibit distinctive intermolecular hydrogen bond systems. In contrast, **3** disposes of only one intermolecular hydrogen bond, and in the crystal structure of **4** none can be found at all, though $\frac{1}{2}H_2O$ is present in the asymmetric unit.

Table 2 summarises the experimentally determined and calculated bond distances and angles of the complexes. The differences between the experimental and theoretically derived data are as expected for the chosen level of theory. Hence, of particular interest is a notable deviation from the virtual linearity of the Ru–N–O fragment in the case of **2**. The value of 171° is 6° smaller than the calculated value. However, the reason obviously is not an artefact of the experiment or calculation, but is due to a close contact of two nitrosyl ligands that are bent away from each other in the crystal structure (Fig. 6).

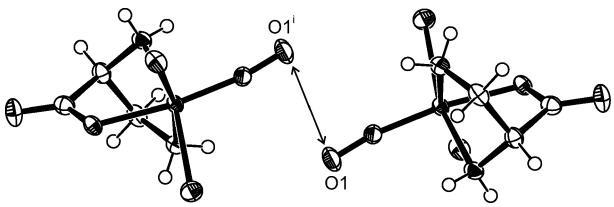

Fig. 6 A centrosymmetric pair of molecules in crystals of **2**. The O1 ··· O1^{i} distance is 2.794(4) Å. Symmetry code: ^{i} $2-x$, $-y$, $1-z$.

Being the most interesting of the five complexes, **1** is compared with the crystal structure of another ruthenium complex, in which L-his is present as a facial tridentate ligand. In [RuCl(L-his)(nbd)] (nbd = norbornadiene),[40] L-his is facially coordinated to Ru with the amino nitrogen sited *trans* to the chlorine atom. As expected, the ruthenium(II) complex disposes of distinctly longer Ru–NH_2 (2.114(8) Å), Ru–$N_{imidazole}$ (2.120(8) Å) and Ru–O (2.114(8) Å) bonds than **1** (see Table 2). The difference is particularly pronounced at the Ru–O bond, as the *trans* influence of NO brings about a comparatively short bond in **1**, whereas the Ru–O bond in [RuCl(L-his)(nbd)] has no nitrosyl but a nbd ligand in the *trans* position.

Table 1 Crystallographic data

	1	2	3	4	5
Empirical formula	$C_6H_8Cl_2N_4O_3Ru$	$C_3H_7Cl_2N_3O_3Ru$	$C_6H_5Cl_3KNO_5Ru$	$C_5H_8Cl_2KN_2O_{5.5}Ru$	$C_4H_6Cl_2KNO_6RuS$
M_r/g mol^{-1}	356.13	305.08	417.63	395.20	407.23
Crystal size/mm	0.11 × 0.08 × 0.03	0.055 × 0.045 × 0.01	0.10 × 0.04 × 0.01	0.18 × 0.05 × 0.04	0.09 × 0.04 × 0.02
T/K	200(2)	200(2)	200(2)	200(2)	200(2)
Crystal system	Orthorhombic	Monoclinic	Triclinic	Monoclinic	Orthorhombic
Space group	$P2_12_12_1$	$P2_1/c$	$P\bar{1}$	$C2/c$	$Pca2_1$
a/Å	8.2032(2)	6.5310(3)	6.7023(2)	28.2438(5)	13.2788(2)
b/Å	10.7355(3)	12.4611(5)	9.6661(4)	6.4321(1)	7.1197(1)
c/Å	12.9656(3)	10.2292(4)	10.7942(5)	13.2528(2)	24.9008(5)
α/°	90	90	71.876(2)	90	90
β/°	90	90.043(2)	84.927(3)	101.9859(9)	90
γ/°	90	90	73.877(2)	90	90
V/Å^3	1141.82(5)	832.49(6)	638.47(4)	2355.11(7)	2354.15(7)
Z	4	4	2	8	8
ρ/g cm^{-3}	2.072	2.434	2.172	2.229	2.298
μ/mm^{-1}	1.838	2.494	2.186	2.149	2.325
Absorption correction	Multi-scan[a]	None[b]	None[b]	None[b]	Multi-scan[a]
T_{min}/T_{max}	0.6338	—	—	—	0.6910
Reflections measured	13 632	3660	5473	7185	24 872
R_{int}	0.0340	0.0361	0.0311	0.0226	0.0392
Mean $\sigma(I)/I$	0.0302	0.0465	0.0410	0.0367	0.0383
θ range/°	3.50–27.48	3.27–27.54	3.16–27.47	3.18–31.12	3.18–27.49
Observed reflections	2485	1563	2467	3151	4702
x, y (weighting scheme)	0.0161, 0.5730	0.0251, 0.2249	0.0268, 0.4330	0.0334, 0.5470	0.0208, 0.3768
Flack parameter	–0.02(3)	—	—	—	–0.02(2)
Reflections in refinement	2614	1903	2899	3764	5300
Parameters	177	137	174	156	306
Restraints	0	6	0	0	7
$R(F_{obs})$	0.0215	0.0298	0.0288	0.0265	0.0248
$R_w(F^2)$	0.0449	0.0648	0.0686	0.0670	0.0502
S	1.084	1.077	1.038	1.053	1.024
Shift/error$_{max}$	0.001	0.001	0.001	0.001	0.003
Max. residual density/e Å^{-3}	0.400	0.98	0.847	0.768	0.459
Min. residual density/e Å^{-3}	–0.653	–0.76	–0.873	–0.809	–0.532

[a] SADABS, v. 2 (G. M. Sheldrick, University of Goettingen, Germany, 2001). [b] SCALEPACK (Z. Otwinowski, W. Minor, in *Methods Enzymol.*, ed. C. W. Carter Jr. and R. M. Sweet, Academic Press, New York, 1997, **276**, 307–326).

NMR Spectroscopy

In **1–3**, the $^{13}C\{^1H\}$-^1H NMR signals were assigned by means of DEPT135, ^1H-^1H-COSY45, ^1H-^{13}C-HMQC and ^1H-^{13}C-HMBC experiments. For **4** and **5**, a starting point for the assignment was needed, as the ligands, mida and tda, are C_s and C_{2v} symmetric, respectively when non-coordinated. By coordination to the $\{RuNO\}^6$ fragment, the symmetry is lifted, which in the $^{13}C\{^1H\}$ spectra of **4** and **5** leads to two signals for the carboxylate as well as for the methylene groups. To assign the signals correctly, DFT calculations for the ^{13}C isotropic magnetic shielding tensors of **1–5** were performed on the PBE1PBE/SDD/aug-cc-pVTZ//B3LYP/SDD/aug-cc-pVDZ and the PBE1PBE/SDD/6–311++G(2d, p)//B3LYP/SDD/6–31G(d, p) levels of theory [short notation: SDD/6–31G(d, p) means SDD basis set for Ru, 6–31G(d, p) for the other atoms]. As a reference, the mean isotropic magnetic shielding tensor of tetramethylsilane was calculated with the respective basis sets. In Table 3, the DFT results are compared with the experimental $^{13}C\{^1H\}$ NMR shifts. Furthermore, the coordination-induced shifts (CISs) of each complex carbon atom in relation to its respective free ligand carbon atom is displayed (in ppm) as $\delta_{complex} - \delta_{free\ ligand}$ ($\Delta\delta$). "Free ligand" means the ligand in the form in which it entered the synthetic procedure, usually the conjugate acid. Altogether the CIS values range from –1.70 to +14.4 ppm.

When compared with experimental data, it shows that the PBE1PBE method affords satisfying calculations of the isotropic magnetic shielding tensors. On average, the application of aug-cc-pVTZ basis sets for non-metal atoms gives slightly higher NMR shifts than the 6–311++G(2d, p) basis sets. The carboxylate-carbon atom's shifts can be assigned unambiguously, though they are marginally underestimated, with a maximum deviation of 2.8 ppm by using aug-cc-pVTZ basis sets. 6–311++G(2d, p) basis sets lead to a maximum deviation of 3.7 ppm. The residual carbon-atom shifts are, for the most part, overrated using both basis sets though the deviation is generally smaller when employing 6–311++G(2d, p) sets. As to **4** and **5**, both basis sets reveal the carboxylate group bonded to the *trans*-NO coordination site as less deshielded than the equatorially-bonded carboxylate. Under that condition, the NMR signals of **4** and **5** were assigned using ^1H-^1H-COSY45, ^1H-^{13}C-HMQC and ^1H-^{13}C-HMBC experiments. Finally, when comparing the DFT results with the respective experimental values, the order of carbon atoms obtained by NMR spectroscopy turns out to be maintained within each calculated complex, the only exception being the interchanged order of C1 and C4 in **3**.

Table 2 Comparison of characteristic interatomic X-ray distances [Å] and angles [°] of complexes **1–5** (standard deviations in parentheses) with values obtained by DFT calculations with the B3LYP method using the SDD basis set for the ruthenium atom and aug-cc-pVDZ basis sets for the non-metal atoms

		1	**2**	**3**	**4**	**5**
Bond distances/Å						
$Ru–N_{NO}$	Exp.	1.726(2)	1.735(3)	1.732(3)	1.7399(18)	1.741(3)
	Calc.	1.736	1.735	1.721	1.729	1.730
N–O	Exp.	1.149(3)	1.146(3)	1.146(3)	1.138(2)	1.142(4)
	Calc.	1.155	1.154	1.158	1.160	1.157
Mean Ru–Cl	Exp.	2.3678	2.3723	2.3634	2.3492	2.3798
	Calc.	2.3879	2.3708	2.4132	2.4144	2.4100
$Ru–O_{ax}$	Exp.	2.0102(19)	2.019(2)	2.0174(19)	2.0252(13)	2.013(2)
	Calc.	2.0386	2.059	2.063	2.0383	2.047
$Ru–O_{eq}$	Exp.	—	—	2.060(2)	2.0561(14)	2.030(2)
	Calc.	—	—	2.133	2.0633	2.077
(Mean) $Ru–N_{aliph.,eq}$	Exp.	2.075(2)	2.085	—	2.0943(15)	—
	Calc.	2.143	2.163	—	2.1844	—
$Ru–N_{arom.,eq}$	Exp.	2.072(2)	—	—	—	—
	Calc.	2.133	—	—	—	—
Ru–S	Exp.	—	—	—	—	2.3232(9)
	Calc.	—	—	—	—	2.4191
Bond angles/°						
Ru–N–O	Exp.	177.7(2)	171.0(3)	175.7(3)	176.55(18)	176.1(3)
	Calc.	175.3	177.1	176.2	175.40	175.5
Mean N_{NO}–Ru–Cl	Exp.	92.66	95.69	93.82	93.95	91.64
	Calc.	93.70	93.93	93.56	91.45	92.11
$N_{NO}–Ru–O_{ax}$	Exp.	178.66(10)	172.29(11)	175.87(11)	176.46(7)	177.59(13)
	Calc.	174.53	175.60	174.94	176.10	177.03
$N_{NO}–Ru–O_{eq}$	Exp.	—	—	94.62(10)	97.08(8)	98.09(12)
	Calc.	—	—	96.05	94.62	95.47
(Mean) $N_{NO}–Ru–N_{aliph.,eq}$	Exp.	98.73(11)	96.95	—	95.75(7)	—
	Calc.	98.24	99.83	—	99.33	—
$N_{NO}–Ru–N_{arom.,eq}$	Exp.	94.63(10)	—	—	—	—
	Calc.	95.89	—	—	—	—
N_{NO}–Ru–S	Exp.	—	—	—	—	96.75(11)
	Calc.	—	—	—	—	96.89

All five novel complexes display some stability against solvolysis in terms of NMR spectra, where in each case only one species is found in solution in the space of about 8 h. The first compound to show signs of hydrolysis after that period of time is **5**, followed by **3**. NMR spectra of the same solutions of **1–5**, re-recorded 7 d later, show no indication of solvolysis as to **1**, **2** and **4**, but, in addition to the signals of **3** and **5**, the signals of one hydrolysis product of the latter compounds. The hydrolysed species of **3** as well as **5** display about the same intensity as the original peaks and, in relation to them, are only marginally shifted on the ppm scale.

IR and UV-vis spectroscopy at room temperature

In Table 4 some of the basic experimental vibrational frequencies (IR bands) and the lowest electronic transition (UV-vis band) of **1–5** are displayed, the former compared with values obtained by B3LYP-based calculations. The calculated vibrational frequencies are multiplied by a scale factor of 0.961 to improve agreement with experiment, leading to comparatively precise values for ν(NO), $\nu_{as}(COO^-)$ and $\delta(NH_2)$.[41] With $\nu_{as}(NH_2)$, $\nu_s(NH_2)$, and ν(OH), it is not surprising that all calculated values are largely overestimated, since intermolecular hydrogen bonds are completely neglected in the gas phase calculations. The recorded ν(NO) values of **1–5** are slightly lower than ν(NO) of the starting material $K_2[Ru(NO)Cl_5]$, which is found at 1898 cm^{-1}. Otherwise, all novel compounds show very similar ν(NO) values among themselves, lying in a range between 1864–1891 cm^{-1}. That fact can probably be attributed to the similar axial coordination as all compounds dispose of an oxygen donor atom in *trans* position to NO.

In the blue range, the UV-vis spectra of **1–5** show weakly permitted transitions (ε = 45–178 mol^{-1} dm^3 cm^{-1}), which are attributed to MLCT bands $d(Ru) \rightarrow \pi^*(NO)$. On the basis of DFT calculations, the lowest energy bands detected in the spectra are assigned to $d_{xy} \rightarrow \pi^*(NO)$ transitions.

Dynamic differential scanning calorimetry

The heat flow of the exothermal decay of the metastable states S1 and S2 is detected as the time derivative of the enthalpy against temperature in a DSC experiment. Fig. 7 shows the results for such a DSC measurement on a powder sample of **2** after irradiation with $\lambda = 457.9$ nm at $T = 100$ K for S1. The state S2 is generated by a two-step procedure: first, the state S1 is generated with blue light ($\lambda = 457.9$ nm) and second, the state S1 is subsequently transferred with infrared light ($\lambda = 1064$ nm) to S2. The decay of the metastable states yields a maximum in the heat flow at T_d = 250 K for S1 and at T_d = 190 K for S2, when a heating rate of $q = 4$ K min^{-1} is used (for the dependence of T_d from the heating

Table 3 $^{13}C\{^{1}H\}$ NMR chemical shifts (in ppm) of the complexes **1–5** and their corresponding free ligands A–E. The coordination induced shift (CIS) (in ppm) is calculated as $\delta_{complex} - \delta_{free\,ligand}$ ($\Delta\delta$). Below each CIS the ^{13}C NMR chemical shifts obtained by DFT calculations using the PBE1PBE method are given (the isotropic magnetic shielding tensor of tetramethylsilane is used as the reference). For notation and atomic numbering see Schemes 2 and 3

		C1	C2	C3	C4	C5	C6
1[a]	δ	178.0	55.5	26.6	131.8	115.9	138.0
A[b]	δ	173.1	53.9	27.3	131.3	115.8	135.4
CIS	$\Delta\delta$	4.9	1.6	–0.7	0.5	0.1	2.6
1 (DFT)[d]		177.4	60.9	32.0	142.3	119.1	143.9
1 (DFT)[e]		176.8	59.5	31.8	141.7	118.1	144.3
2[a]	δ	175.0	63.7	43.5	—	—	—
B[b]	δ	170.1	49.3	37.8	—	—	—
CIS	$\Delta\delta$	4.9	14.4	5.7	—	—	—
2 (DFT)[d]		173.9	65.5	49.2	—	—	—
2 (DFT)[e]		173.4	65.4	48.8	—	—	—
3[c]	δ	157.7	184.7	109.5	171.1	144.9	60.5
C[c]	δ	145.4	177.3	111.2	169.2	142.6	60.5
CIS	$\Delta\delta$	12.3	7.4	–1.7	1.9	2.3	0.0
3 (DFT)[d]		169.2	190.6	110.8	168.6	143.0	66.9
3 (DFT)[e]		169.1	190.2	110.1	168.0	142.4	65.8
4[c]	δ	180.2	69.6	69.0	183.6	55.5	—
D[c]	δ	169.7	57.9	57.9	169.7	43.2	—
CIS	$\Delta\delta$	10.5	11.7	11.1	13.9	12.3	—
4 (DFT)[d]		180.2	74.6	67.5	182.9	52.9	—
4 (DFT)[e]		179.3	72.6	69.7	181.4	52.7	—
5[c]	δ	179.8	42.8	40.0	183.5	—	—
E[c]	δ	174.6	34.6	34.6	174.6	—	—
CIS	$\Delta\delta$	5.2	8.2	5.4	8.9	—	—
5 (DFT)[d]		179.0	48.9	43.1	180.7	—	—
5 (DFT)[e]		178.2	49.7	42.4	179.8	—	—

[a] [D6]DMSO as the solvent. [b] D_2O as the solvent, [D_6]DMSO capillary tube as reference. [c] D_2O as the solvent, acetone as reference. [d] SDD for ruthenium, aug-cc-pVTZ for non-metal atoms. [e] SDD for ruthenium, 6–311++G(2d, p) for non-metal atoms.

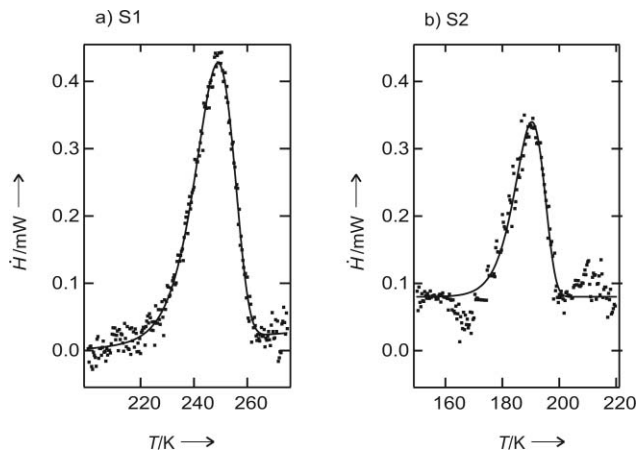

Fig. 7 Heat flow from PLI in **2** observed after illumination at T = 100 K; (a) S1 illuminated with 457.9 nm; (b) S2 illuminated with 457.9 nm and subsequently with 1064 nm. Lines are fits according to eqn (1). The resulting fit parameters are given in Table 5.

rate see ref. 42). The activation energy E_A and the frequency factor Z of the single exponential decays of S1 and S2 are determined by fitting the measured data (eqn (1) in the Experimental). The fitted parameters are summarised in Table 5. The error in the determination of the frequency factors Z is about one order of magnitude due to the small temperature range of the decay.

Analogous DSC measurements were performed for the other compounds of this work. The results are summarised in Table 5. Signals of the thermal decay of S1 were detected for **1–4** while signals due to the decay of S2 were detected in **1** and **2** using the procedure described above. Illumination of **5** with wavelengths in the range of 430–514 nm did not result in any measurable thermal signal of metastable states, the detection limit of the DSC apparatus used being about 0.3 kJ mol^{-1}. For the generation of S2, we applied the usually successful procedure of first generating S1 with blue-green light and then transferring S1 into S2 with infrared light.[22] This proved successful for samples of **1** and **2**. In samples of **3** the population of S1 was too low to obtain a measurable fraction of S2 *via* this transfer procedure. In the case of **4**, there was enough S1 for transfer into S2. However, by illuminating **4** in the S1 state with 1064 nm we observed only the decrease of the S1 population without the appearance of any new heat flow from S2. The depopulation of S1 at 1064 nm irradiation is rather fast and is completed within the exposure of $Q = 2.2$ J cm^{-2}.

Low-temperature infrared spectroscopy

Fig. 8 shows the infrared spectrum of **2** in the range of 1500–2000 cm^{-1} (a) in the GS at T = 85 K, (b) after irradiation with λ = 457.9 nm at T = 85 K, and (c) subsequent irradiation with 1064 nm at T = 85 K. We observe shifts of the NO stretching vibration from 1872–1879 cm^{-1} in GS to 1749–1740 cm^{-1} in S1 and to 1562 cm^{-1} in S2. The area of this band of GS is proportional to the number of molecules in GS. Therefore, its decrease after irradiation is a measure of the population P of S1 and S2. In **2**, a population of P = 21% of S1 and 12% of S2 was reached. Using the totally released enthalpy H_{tot} determined by DSC (see Table 5) we calculated the energetic position E of the metastable linkage isomers with respect to the GS by using $H_{tot} = P \times E$. In

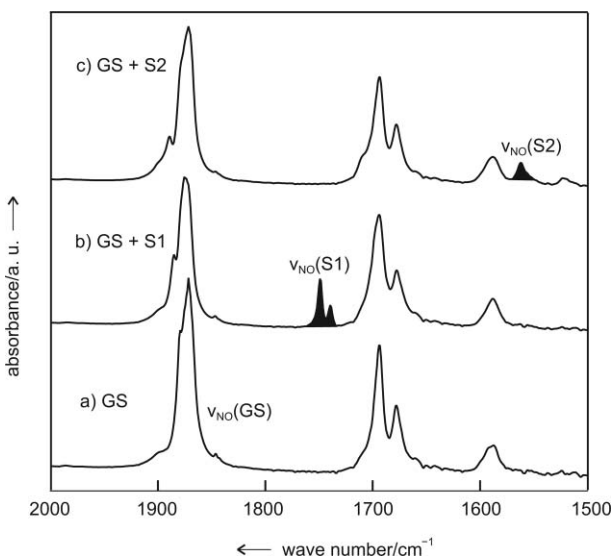

Fig. 8 Infrared spectra of **2** (a) in GS at T = 85 K, (b) after illumination with 457.9 nm at T = 85 K (b), and (c) after illumination with 457.9 nm and 1064 nm at T = 85 K. The stretching vibration ν_{NO} shifts from (a) 1879/1872 cm^{-1} in GS to (b) 1749/1740 cm^{-1} in S1 and (c) to 1562 cm^{-1} in S2. From the decrease of the area of the ν_{NO}(GS) band the population P of S1 and S2 can be determined. Results are given in Table 6. Spectra are shifted vertically for clarity, but have the same scale.

Table 4 Comparison of basic experimental vibrational frequencies (cm^{-1}) of the complexes **1–5** (room temperature, solid samples, single-reflection ATR diamond plate) with values obtained by DFT calculations at the B3LYP level of theory (SDD basis set for the ruthenium atom and aug-cc-pVDZ basis set for the non-metal atoms) and assignment of the $d_{xy} \rightarrow \pi^*(NO)$ electronic transition to the respective low-energy UV-vis band (nm) (IR: m = medium, s = strong, vs = very strong, br = broad; UV-vis: sh = shoulder, ε/mol^{-1} dm^3 cm^{-1} in parentheses)

		1	**2**	**3**	**4**	**5**
IR bands/cm^{-1}						
ν(NO)	Exp.	1891 (vs)	1864 (vs)	1878 (vs)	1870 (vs)	1878 (vs) 1869 (vs)
	Calc.	1861	1865	1852	1837	1850
$\nu_{as}(COO^-)$	Exp.	1658 (vs)	1690 (s) 1674 (s)	—	1630 (vs, br)	1659 (vs) 1633 (vs) 1611 (vs)
	Calc.	1682	1696		1663 1641	1652 1632
$\nu_{as}(NH_2)$	Exp.	3205 (m)	3234 (m) 3222 (m)	—	—	—
	Calc.	3383	3414 3393			
$\nu_s(NH_2)$	Exp.	3122 (m)	3112 (m) 3059 (m)	—	—	—
	Calc.	3266	3327 3303			
$\delta(NH_2)$	Exp.	1600 (m)	1583 (m)	—	—	—
	Calc.	1567	1569 1565			
ν(OH)	Exp.	—	—	3394 (m)	—	—
	Calc.			3794		
UV-vis/nm (mol^{-1} dm^3 cm^{-1})						
$d_{xy} \rightarrow$ *(NO)	Exp.	459 (sh) (59)	475 (sh) (45)	478 (128)	416 (160)	430 (178)

Table 5 Activation energies and frequency factors of PLI in **1–5**, n.a. = not available

	E_A(S1)/eV	Z_{S1}/s^{-1}	H_{tot}(S1)/ kJ mol^{-1}	E_A(S2)/eV	Z_{S2}/s^{-1}	H_{tot}(S2)/ kJ mol^{-1}
1	0.67(3)	1×10^{13}	13.3	0.51(4)	3×10^{11}	7
2	0.72(3)	3×10^{12}	23.6	0.59(3)	5×10^{13}	10.6
3	0.57(5)	1×10^{12}	1	n.a.	n.a.	n.a.
4	0.60(3)	2×10^{12}	8.3	n.a.	n.a.	n.a.
5	n.a.	n.a.	n.a.	n.a.	n.a.	n.a.

Table 6 Wavenumbers of stretching vibrations ν_{NO} (cm^{-1}) and population P of linkage isomers obtained from infrared spectroscopy. The energetic positions E of the linkage isomers are calculated from the observed population P and the corresponding heat flow H_{tot} from DSC measurements (see Table 5); n.a. = not available. The number in parentheses at P_{S1} is the respective excitation wavelength (nm)

	ν_{NO}(GS)	ν_{NO}(S1)	ν_{NO}(S2)	P_{S1}/%	E_{S1}/eV	P_{S2}/%	E_{S2}/eV
1	1900	1768	1537	11.6 (476)	1.19	4.0	1.82
2	1879/1872	1749/1740	1562	21 (458)	1.16	12	0.92
3	1888	1748	n.a.	1.4 (476)	1.45	n.a.	n.a.
4	1879	1738	n.a.	5.7 (476)	1.54	n.a.	n.a.
5	1884	1762	n.a.	1.7 (496)	n.a.	n.a.	n.a.

this manner, we obtained $E_{S1} = 1.16$ eV and $E_{S2} = 0.92$ eV for **2**. Similar results were obtained for the other samples (Table 6). Notably, we have detected the state S1 also for **5**, though with a very low population of 1.7%. Hence, we have determined by DSC and IR spectroscopy the characteristic points of the potential surface, which could now be compared with calculations from DFT. Note that for the calculation of the energetic positions we assume that the decay of the PLI is completely radiationless, *i.e.*, all the heat is given to the lattice.

A special feature occurs in **1**, where the energetic position of state S2 is by 0.63 eV higher than that of state S1. This was observed up to now only in the compound $Na_2[OsCl_5(NO)]\cdot H_2O$.[43] As the authors report, the state S2 can therefore thermally decay into S1 instead of GS. Such a thermal occupation of S1 should then appear as heat flow during the measurement of the thermal decay of S2. However, we observed only the decay signal of S2 at 191 K and no further signal at 222 K, where the signal of S1 is expected. In contrast to the osmate, the S2 state of **1** thus relaxes directly into the ground state.

Conclusions

In a bioligand approach to nitrosyl–ruthenium chemistry, five complexes have been synthesised and characterised by single-crystal X-ray diffraction analysis, mass spectrometry, spectroscopic methods (NMR, UV-vis, IR) and elemental analysis. All five complexes display some stability against solvolysis in terms of NMR spectra, where in each case only one species is found in solution in the space of about 8 h. The first compound to show signs of hydrolysis after that period of time is **5**, followed by **3**. Even after a period of 7 d, there is no indication of solvolysis as to **1**, **2** and **4**.

1–5 exhibit common features: in all compounds, a (vinylogous) carboxylate function is *trans* to the nitrosyl ligand, and the equatorial plane contains at least two chlorido ligands. Attempts to generate photoinduced metastable states by irradiation into

the Ru → π*(NO) transition were successful for all compounds. As a main result, we find that the isonitrosyl state S1 can be generated and detected in all samples, even though the reachable population in samples **3–5** is very low. The side-on state S2 is detected only in **1** and **2**. In **1–5** considerable differences arise as to the degree of population of the metastable state S1. The reason is presumably found in the first coordination sphere of the {RuNO}^{6} moiety. The highest population of 21% is achieved in **2**, where two NH_2 groups without any π contributions complete the equatorial plane. In **1**, one of the NH_2 groups is exchanged for an aromatic imidazol ring with potential π contributions, whereby the population is decreased to about 12%. It should be mentioned, however, that the imidazole ring is twisted against the complex's equatorial plane spanned by Cl1–Ru–Cl2 by circa 30°, thus lacking proper co-planarity. In **4**, the two NH_2 groups of **1** are replaced by a tertiary nitrogen atom with σ-donor abilities, and an oxygen atom with π effects. This leads to a further decrease of the reachable S1 population down to about 6%. Finally, in **3** and **5**, the remaining tertiary nitrogen atom of **4** is replaced by a chlorido and a sulfur ligand, respectively, yielding the maximum number of four π interacting ligands in the equatorial plane. This leads to an almost complete breakdown of the S1 population.

Our results support other (literature) data on the assumption that the population of metastable states increase if the *cis* ligands do not exhibit π effects: it has been estimated that salts of the $[Ru(NO)(NH_3)_5]^{3+}$ ion achieve populations of up to 16% in S1,[22] whereas powdered/microcrystalline samples of the complex $K_2[Ru(NO)Cl_5]$ can be populated only up to 1–2%.[30] For *trans*-$[Ru(NO)(NH_3)_4Cl]^{2+}$, intermediate values were found,[31] thus underlining that not only the *trans*-bonded ligand but also the equatorial coordination sphere is decisive for the PLI characteristics of a species. Maximum values for the population of structurally excited states (76% for S1) have recently been reported for another *trans*-chlorido complex, the fluoridoborate hemihydrate of the *trans*-$[Ru(NO)(py)_4Cl]^{2+}$ ion (py = pyridine).[32] As in the amine complex $[Ru(NO)(NH_3)_5]^{3+}$, no notable π contributions have to be assigned to the ruthenium–pyridine bonds due to the lack of co-planarity of the aromatic rings and the complex's equatorial plane.

With the experimental PLI data on **1–5** at hand, an extensive DFT study on the five complexes with a special focus on **2** has been started centering on the contribution of the σ- and π-donating chlorido and the purely σ-donating nitrogen donors on the PLI process.

Experimental

Materials

$RuCl_3 \cdot xH_2O$, L-histidine hydrochloride monohydrate, thiodiacetic acid and methyliminodiacetic acid were used as supplied by Sigma-Aldrich. Kojic acid, *rac*-3-amino-alanine monohydrochloride, KCl, KNO_2, HCl (37%) and potassium hydroxide were purchased from Fluka and used without further purification. Ethanol, diethyl ether and 0.1 M HCl were used as supplied by Merck. $K_2[Ru(NO)Cl_5]$ was prepared according to a literature procedure.[44] All the described compounds are stable in air.

General information

Computational details

The Gaussian 03 program package[45] was used for all calculations. For ruthenium, the SDD basis set[46,47] was used, which resorts to the effective Stuttgart/Dresden core potential (SD) and the Dunning/Huzinaga double zeta valence basis set (D95V) (16 electrons in valence shell). Structures were optimized with the B3LYP hybrid method[48–52] and either the Dunning correlation consistent basis set[53] aug-cc-pVDZ or the Pople type basis set[54] 6–31G(d, p) for all atoms except ruthenium. Found stationary points were confirmed with subsequent frequency analysis on the corresponding level of theory. NMR spectra were predicted by single point calculations with the hybrid functional PBE1PBE[55,56] and either the Dunning correlation consistent basis set[53] aug-cc-pVTZ on geometries optimized with B3LYP/aug-cc-pVDZ or the Pople type basis set[54] 6–311++G(2d, p) on geometries optimized with B3LYP/6–31G(d, p). The calculations with Pople basis sets were initially conducted for NMR prediction. As expected, geometries and predicted NMR shifts do not differ much from those calculated with correlation-consistent basis sets.

NMR spectroscopy

NMR spectra were recorded at room temperature on Jeol Eclipse 270 (^{1}H: 270 MHz, ^{13}C{^{1}H}: 67.9 MHz) and Jeol Eclipse 400 (^{1}H: 400 MHz, ^{13}C{^{1}H}: 101 MHz) NMR spectrometers. The signals of the deuterated solvent (^{13}C{^{1}H}) and the residual protons therein (^{1}H) were used as an internal secondary reference for the chemical shift. When D_2O was used as a solvent either one drop of acetone or a small capillary tube containing [D_6]DMSO were added to the sample tube (5 mm) in order to obtain a reference signal in the ^{13}C{^{1}H} NMR spectra. When necessary the ^{1}H and ^{13}C{^{1}H} NMR signals were assigned by means of ^{1}H-^{1}H-COSY45, DEPT135, ^{1}H-^{13}C-HMQC, and ^{1}H-^{13}C-HMBC experiments. For atom numbering see Scheme 3.

Mass spectrometry

Mass spectra were measured on a Thermo Finnigan LTQ FT with IonMax (ion source with ESI head).

Differential scanning calorimetry

The thermodynamic measurements were performed by differential scanning calorimetry (DSC) using a Mettler DSC 30 equipped with two quartz windows inside and outside of the cryostat for light irradiation. The powder in an aluminium crucible was irradiated by the monochromatic light of an argon laser at 457.9, 476.5, 488, 496.5 or 514 nm for the population of the metastable state S1. The transfer from S1 to S2 was performed with light of a Nd:YAG laser at 1064 nm after S1 had been previously generated up to saturation with blue-green light. The light exposure $Q = \int I(t)\mathrm{d}t$ on the sample is given by the integral over the product of light intensity I and irradiation time t. The dynamic measurements were performed with a linear heating rate of $q = \mathrm{d}T/\mathrm{d}t = 4$ K min^{-1}. The corresponding spectrum of the un-irradiated sample was subtracted to reach a horizontal baseline in the temperature range of the thermal decay. The detected signal of the DSC (heat flow)

is the time derivative of the enthalpy dH/dt in mW over the temperature. The total enthalpy of the decay is given by integration over time or temperature. The activation energy E_A and the frequency factor Z of the Arrhenius-like decay are obtained by fitting the measured data to the equation:

$$\dot{H} = \frac{dH(T)}{dt} = H_{tot} Z \exp\left\{ -\frac{E_A}{k_B T} - \frac{Z}{q} \int_{T_0}^{T} \exp\left(-\frac{E_A}{k_B T'} \right) \right\} \quad (1)$$

where k_B denotes the Boltzmann constant, q the heating rate and T_0 the starting temperature for the integration. The integration is performed numerically over the temperature range of the decay. The samples were irradiated at $T = 100$ K in an N_2 atmosphere. Further details concerning the evaluation of the DSC results are described in ref. 23.

UV-vis and IR spectroscopy at room temperature

UV-vis: Varian Cary 50 Bio (10-mm quartz glass cuvettes); IR: Jasco FT/IR-460plus equipped with a single-reflection ATR diamond plate (solid samples).

Infrared spectroscopy at low temperature

The infrared spectra were collected with a Nicolet 5700 FTIR spectrometer. The powdered samples were mixed with KBr and pressed as pellets. The KBr pellets were mounted on a copper cold finger using silver paste for good thermal contact. The samples were cooled to 85 K in a liquid-nitrogen cryostat. KBr windows allowed the irradiation of the sample with laser light and absorption measurements down to 390 cm^{-1}. Irradiation was performed with lasers as described above.

Crystal structure determination and refinement†

Crystals suitable for X-ray crystallography were selected with the aid of a polarisation microscope, mounted on the tip of a glass fibre and investigated at 200 K on a Nonius KappaCCD diffractometer with graphite-monochromated MoKα radiation ($\lambda = 0.71073$ Å). The structures were solved by direct methods (SIR97) and refined by full-matrix least-squares calculations on F^2 (SHELXL-97). Anisotropic displacement parameters were refined for all non-hydrogen atoms. Crystallographic data are listed in Table 1.

Synthesis

[Ru(NO)Cl$_2$(L-his)] (1). $K_2[Ru(NO)Cl_5]$ (658 mg, 1.70 mmol), L-histidine hydrochloride monohydrate (358 mg, 1.71 mmol) and KCl (1.26 g, 16.9 mmol) were dissolved in 250 mL H_2O. The pH-value of the solution was adjusted to 4 with 0.1 M HCl. After refluxing for 2 h, the resulting light brown solution was evaporated to dryness on a rotary evaporator. The residue was suspended in a small amount of H_2O and purified by centrifugation (3 times). Then, the resulting brown solid was vacuum-dried (234 mg, 0.641 mmol, 37.7% yield). Crystals suitable for X-ray crystallography were obtained from a diluted aqueous solution of the complex by slow evaporation of the solvent at room temperature. ^{1}H NMR (399.78 MHz, [D$_6$]DMSO, 23 °C) δ/ppm: 13.27 (s, 1H, H8), 8.29 (s, 1H, H6), 7.29 (s, 1H, H5), 6.83–6.80 (m, 1H, H7b), 6.53 (d, ^2J(H7a, H7b) = 9.4 Hz, 1H, H7a), 3.94 (pseudo q = ddd, ^3J(H2, H3a) ≈ ^3J(H2, H3b) ≈ ^3J(H2, H7b) ≈ 2–4 Hz, 1H, H2), 3.28 (partially superposed by the H_2O signal) (dd, ^2J(H3a, H3b) ≈ 17–19 Hz, ^3J(H3a/b, H2) ≈ 2 Hz, 1H, H3a/3b), 3.13 (ddd, ^2J(H3a, H3b) = 17.4 Hz, ^3J(H3a/3b, H2) = 4.1 Hz, ^4J(H3a/3b, H7b/5) = 1.4 Hz). ^{13}C NMR (100.53 MHz, [D$_6$]DMSO, 25 °C) δ/ppm: 178.0 (C1), 138.0 (C6), 131.8 (C4), 115.9 (C5), 55.5 (C2), 26.6 (C3). Selected IR bands ν_{max}/cm^{-1}: 3264 (vw, br), 3205 (m), 3122 (m), 3034 (vw), 2955 (vw), 2906 (vw), 2849 (vw), 1891 (vs), 1658 (vs), 1600 (m), 1577 (m), 1498 (w), 1460 (w), 1434 (m), 1374 (m), 1302 (m), 1269 (w), 1184 (m), 1161 (s), 1086 (m), 996 (w), 911 (w), 899 (w), 833 (w), 716 (m), 680 (w), 621 (s). UV-vis (DMSO) λ_{max}/nm (ε/mol^{-1} dm^3 cm^{-1}): 459 (sh.) (59), 348 (sh.) (239). MS-ESI (negative ions, H_2O–CH_3CN = 90 : 10): m/z calcd. for $C_6H_7Cl_2N_4O_3Ru$ = $[M - H]^-$ 354.9, found 354.9 with a characteristic Ru_1 pattern; m/z calcd. for $C_{12}H_{15}Cl_4N_8O_6Ru_2$ = $[2M - H]^-$ 712.8, found 712.8 with a characteristic Ru_2 pattern; m/z calcd. for $C_{12}H_{16}Cl_5N_8O_6Ru_2$ = $[2M + Cl]^-$ 748.8, found 748.8 with a characteristic Ru_2 pattern. Elemental analysis (%) calcd. for $C_6H_8Cl_2N_4O_3Ru \cdot 0.5\ H_2O$ (365.14) (the existence of 0.5 equiv. of H_2O in the amorphous compound was proved by thermogravimetric measurements showing a mass decrease of 2.44% in the temperature range of 25–250 °C, which is in agreement with the expected value of 2.47%) C 19.74, H 2.48, Cl 19.42, N 15.34. Found: C 19.83, H 2.45, Cl 19.68, N 15.37.

[Ru(NO)Cl$_2$(*rac*-dap)] (2). $K_2[Ru(NO)Cl_5]$ (802 mg, 2.08 mmol), *rac*-3-amino-alanine hydrochloride (584 mg, 4.15 mmol) and KCl (1.55 g, 20.8 mmol) were dissolved in 250 mL H_2O. The pH-value of the solution was adjusted to 4 with a concentrated solution of KOH in H_2O. Then the mixture was refluxed for 2 h and the resulting orange solution was evaporated to dryness on a rotary evaporator. The residue was suspended in a small amount of H_2O and purified by centrifugation (3 times). Then the resulting orange solid was vacuum-dried (244 mg, 0.800 mmol, 38.5% yield). Crystals suitable for X-ray crystallography were obtained by heating the solid in H_2O until a clear solution resulted, which was slowly cooled down to room temperature. Within a day, small orange crystals precipitated from the solution. ^{1}H NMR (400.18 MHz, [D$_6$]DMSO, 25 °C) δ/ppm: 6.87 (d, ^2J(H5a, H5b) = 7.9 Hz, 1H, H5a/b), 6.34–6.35 (m, 1H, H4a/b), 6.32–6.24 (m, 2H, H4a/b + H5a/b), 3.61 (s, 1H, H2), 2.91–2.81 (m, 2H, H3a + H3b). ^{13}C NMR (100.63 MHz, [D$_6$]DMSO, 25 °C) δ/ppm: 175.0 (C1), 63.7 (C2), 43.5 (C3). Selected IR bands ν_{max}/cm^{-1}: 3234 (m), 3222 (m), 3112 (m), 3059 (m), 2970 (vw), 1864 (vs), 1690 (s), 1674 (s), 1583 (m), 1369 (m), 1265 (m), 1218 (m), 1127 (s), 1027 (m), 993 (m), 909 (m), 864 (m), 790 (m), 746 (m), 611 (m). UV-vis (DMSO) λ_{max}/nm (ε/mol^{-1} dm^3 cm^{-1}): 475 (sh.) (45), 391 (216), 362 (205). MS-ESI (negative ions, H_2O–CH_3CN = 90 : 10): m/z calcd. for $C_3H_6Cl_2N_3O_3Ru$ = $[M - H]^-$ 303.9, found 303.9 with a characteristic Ru_1 pattern; m/z calcd for $C_3H_7Cl_3N_3O_3Ru$ = $[M + Cl]^-$ 341.9, found 341.9 with a characteristic Ru_1 pattern; m/z calcd. for $C_6H_{13}Cl_4N_6O_6Ru_2$ = $[2M - H]^-$ 610.8, found 610.8 with a characteristic Ru_2 pattern; m/z calcd. for $C_6H_{14}Cl_5N_6O_6Ru_2$ = $[2M + Cl]^-$ 646.8, found 646.7 with a characteristic Ru_2 pattern; m/z calcd. for $C_9H_{20}Cl_6N_9O_9Ru_3$ = $[3M - H]^-$ 914.7, found 914.7 with a characteristic Ru_3 pattern; m/z calcd. for $C_9H_{21}Cl_7N_9O_9Ru_3$ = $[3M + Cl]^-$ 951.7, found 951.6 with a characteristic Ru_3 pattern. Elemental analysis (%) calcd. for

$C_3H_7Cl_2N_3O_3Ru$ (305.08): C 11.81, H 2.31, Cl 23.24, N 13.77. Found: C 11.69, H 2.41, Cl 23.10, N 13.61.

K[Ru(NO)Cl$_3$(koj)] (3). $K_2[Ru(NO)Cl_5]$ (355 mg, 0.918 mmol) and kojic acid (130 mg, 0.915 mmol) were dissolved in 100 mL H_2O. The pH-value of the solution was adjusted to about 5 with a concentrated solution of KOH in H_2O, then the mixture was refluxed for 1 h. The resulting brown solution was filtered and evaporated to dryness on a rotary evaporator. The residue was dissolved in 2.5 mL H_2O. Slow evaporation of the solvent yielded brown crystals which were filtered, washed with 2–3 mL H_2O and 50 mL diethylether, and vacuum-dried (83 mg, 0.198 mmol, 21.6% yield). ^{1}H NMR (399.78 MHz, D_2O, 22 °C) δ/ppm: 8.19 (s, 1H, H5), 6.99 (s, 1H, H3), 4.57 (s, 2H, H6). ^{13}C NMR (100.53 MHz, D_2O, 25 °C) δ/ppm: 184.7 (C2), 171.1 (C4), 157.7 (C1), 144.9 (C5), 109.5 (C3), 60.5 (C6). Selected IR bands ν_{max}/cm^{-1}: 3394 (m), 3092 (vw), 3070 (vw), 2912 (vw), 2869 (vw), 1878 (vs), 1607 (m), 1559 (s), 1504 (s), 1485 (s), 1445 (m), 1400 (m), 1379 (w), 1343 (w), 1271 (m), 1229 (m), 1191 (m), 1151 (m), 1052 (m), 975 (w), 930 (m), 863 (m), 833 (m), 796 (m), 770 (m), 655 (m). UV-vis (H_2O) λ_{max}/nm (ε/mol^{-1} dm^3 cm^{-1}): 478 (128), 312 (8036), 254 (sh.) (12 762). MS-ESI (negative ions, H_2O–CH_3CN = 90 : 10): *m*/*z* calcd. for $C_6H_5Cl_3NO_5Ru$ = [M (without K$^+$)]$^-$ 379.8, found 379.8 with a characteristic Ru_1 pattern; MS-ESI (positive ions, H_2O–CH_3CN = 90 : 10): *m*/*z* calcd. for $C_6H_5Cl_3K_2NO_5Ru$ = [M + 2K]$^+$ 457.8, found 457.8 with a characteristic Ru_1 pattern. Elemental analysis (%) calcd. for $C_6H_5Cl_3KNO_5Ru{\cdot}1/7H_2O$ (420.21) (the existence of 1/7 equivalents of H_2O in the compound was confirmed by thermogravimetric measurements showing a mass decrease of 0.59% in the temperature range of 25–250 °C, which was in agreement with the expected value of 0.61%) C 17.15, H 1.27, Cl 25.31, N 3.33. Found: C 17.20, H 1.30, Cl 25.04, N 3.29.

K[Ru(NO)Cl$_2$(mida)]·$\frac{1}{2}$H$_2$O (4). $K_2[Ru(NO)Cl_5]$ (515 mg, 1.33 mmol) was suspended in 100 mL ethanol–H_2O (3 : 1), then methyliminodiacetic acid (196 mg, 1.33 mmol) was dissolved in 5 mL H_2O and added dropwise to the suspension. The pH-value of the suspension was adjusted to 5 with a concentrated solution of KOH in H_2O, then the mixture was refluxed for 2 h. The resulting brown solution was filtered and evaporated to dryness on a rotary evaporator. Under heating, the residue was dissolved in 6 mL H_2O and filtered again. Within a day, small brown crystals precipitated, which were filtered, washed with 4 mL ethanol–H_2O (3 : 1) and 50 mL diethylether, and vacuum-dried (214 mg, 0.541 mmol, 40.7% yield). ^{1}H NMR (399.78 MHz, D_2O, 22 °C) δ/ppm: 4.21 (dd, ^2J(H2a, H2b) ≈ 16–17 Hz, ^4J(H2a, H3a) ≈ 1–2 Hz, 1H, H2a), 4.19 (dd, ^2J(H3a, H3b) ≈ 17–18 Hz, ^4J(H3a, H2a) ≈ 1–2 Hz, 1H, H3a), 3.93 (d, ^2J(H3b, H3a) = 17.6 Hz, 1H, H3b), 3.72 (d, ^2J(H2b, H2a) = 16.8 Hz, 1H, H2b), 3.04 (s, 3H, H5). ^{13}C NMR (100.53 MHz, D_2O, 24 °C) δ/ppm: 183.6 (C4), 180.2 (C1), 69.6 (C2), 69.0 (C3), 55.5 (C5). Selected IR bands ν_{max}/cm^{-1}: 3564 (w, br), 2980 (w), 2932 (w), 1870 (vs), 1630 (vs, br), 1460 (m), 1440 (m), 1366 (s), 1349 (m), 1318 (s), 1305 (s), 1254 (m), 1152 (w), 1084 (w), 986 (m), 941 (m), 923 (m), 900 (s), 752 (m), 615 (m), 602 (m). UV-vis (H_2O) λ_{max}/nm (ε/mol^{-1} dm^3 cm^{-1}): 416 (160), 353 (sh.) (227). MS-ESI (negative ions, H_2O–CH_3CN = 90 : 10): *m*/*z* calcd. for $C_5H_7Cl_2N_2O_5Ru$ = [M (without K$^+$)]$^-$ 346.9, found 346.9 with a characteristic Ru_1 pattern. Elemental analysis (%) calcd. for $C_5H_7Cl_2KN_2O_5Ru{\cdot}0.5H_2O$ (395.21) (the existence of 0.5 equiv. of H_2O in the crystalline compound was confirmed by X-ray diffraction analysis and thermogravimetric measurements showing a mass decrease of 2.38% in the temperature range of 25–280 °C, which is in agreement with the expected value of 2.28%) C 15.20, H 2.04, Cl 17.94, N 7.09. Found: C 15.18, H 2.10, Cl 17.78, N 7.14.

K[Ru(NO)Cl$_2$(tda)]·H$_2$O (5). $K_2[Ru(NO)Cl_5]$ (500 mg, 1.29 mmol) was suspended in 200 mL ethanol–H_2O (3 : 1), then a solution of thiodiglycolic acid (194 mg, 1.29 mmol) and KOH (145 mg, 2.58 mmol) in 7 mL H_2O was added dropwise. The mixture was refluxed for 1 h, filtered and evaporated to dryness on a rotary evaporator. The residue was dissolved in 2.5 mL H_2O. Slow evaporation of the solvent yielded brown crystals which were filtered, washed with 20 mL ethanol–H_2O (3 : 1) and 100 mL diethylether and vacuum-dried (128 mg, 0.314 mmol, 24.3% yield). ^{1}H NMR (399.78 MHz, D_2O, 22 °C) δ/ppm: 4.13 (d, ^2J(H2a, H2b) = 17.3 Hz, 1H, H2a/b), 4.08 (d, ^2J(H3a, H3b) = 17.8 Hz, 1H, H3a/b), 3.86 (d, ^2J(H2a, H2b) = 17.3 Hz, 1H, H2a/2b), 3.83 (d, ^2J(H3a, H3b) = 17.8 Hz, 1 H, H3a/3b). ^{13}C NMR (100.53 MHz, D_2O, 24 °C) δ/ppm: 183.5 (C4), 179.8 (C1), 42.8 (C2), 40.0 (C3). Selected IR bands ν_{max}/cm^{-1}: 3578 (w, br), 2989 (w), 2917 (w), 1878 (vs), 1869 (vs), 1659 (vs), 1633 (vs), 1611 (vs), 1377 (w), 1304 (s), 1288 (s), 1244 (m), 1216 (w), 1175 (m), 1144 (m), 931 (s), 923 (s), 865 (w), 772 (w), 728 (m), 619 (m), 603 (m). UV-vis (H_2O) λ_{max}/nm (ε/mol^{-1} dm^3 cm^{-1}): 430 (178). MS-ESI (negative ions, H_2O–CH_3CN = 90 : 10): *m*/*z* calcd. for $C_4H_4Cl_2NO_5RuS$ = [M (without K$^+$)]$^-$ 351.8, found 351.8 with a characteristic Ru_1 pattern. Elemental analysis (%) calcd. for $C_4H_4Cl_2KNO_5RuS{\cdot}H_2O$ (407.23) (the existence of 1 equiv. of H_2O in the crystalline compound was confirmed by X-ray diffraction analysis and thermogravimetric measurements showing a mass decrease of 4.55% in the temperature range of 25–200 °C, which is in agreement with the expected value of 4.43%) C 11.80, H 1.49, Cl 17.41, N 3.44, S 7.87. Found: C 11.81, H 1.54, Cl 17.41, N 3.45, S 7.96.

Acknowledgements

D. S.'s and T. W.'s work was supported by the BMBF (grant FKZ 03 × 5510) and the Deutsche Forschungsgemeinschaft (grants SCHA1550/1–1 and DFG WO618/8–1).

References

1 L. J. Ignarro, *Hypertension (Dallas)*, 1990, **16**, 477–483.
2 A. Calver, J. Collier and P. Vallance, *Exp. Physiol.*, 1993, **78**, 303–326.
3 S. H. Snyder and D. S. Bredt, *Sci. Am.*, 1992, **266**, 68–71.
4 E. Culotta and D. E. Koshland, *Science*, 1992, **258**, 1862–1865.
5 J. S. Stamler, D. J. Singel and J. Loscalzo, *Science*, 1992, **258**, 1898–1902.
6 L. J. Ignarro, *Angew. Chem., Int. Ed.*, 1999, **38**, 1882–1892.
7 G. Stochel, A. Wanat, E. Kulis and Z. Stasicka, *Coord. Chem. Rev.*, 1998, **171**, 203–220.
8 K. Karidi, A. Garoufis, A. Tsipis, N. Hadjiliadis, H. den Dulk and J. Reedijk, *Dalton Trans.*, 2005, 1176–1187.
9 P. C. Ford, *Acc. Chem. Res.*, 2008, **41**, 190–200.
10 P. C. Ford and S. Wecksler, *Coord. Chem. Rev.*, 2005, **249**, 1382–1395.
11 P. C. Ford, J. Bourassa, K. Miranda, B. Lee, I. Lorkovic, S. Boggs, S. Kudo and L. Laverman, *Coord. Chem. Rev.*, 1998, **171**, 185–202.
12 A. K. Patra and P. K. Mascharak, *Inorg. Chem.*, 2003, **42**, 7363–7365.
13 M. J. Rose, M. M. Olmstead and P. K. Mascharak, *J. Am. Chem. Soc.*, 2007, **129**, 5342–5343.
14 G. M. Halpenny, M. M. Olmstead and P. K. Mascharak, *Inorg. Chem.*, 2007, **46**, 6601–6606.

15 J. M. Slocik and R. E. Shepherd, *Inorg. Chim. Acta*, 2000, **311**, 80–94.
16 U. Hauser, V. Oestreich and H. D. Rohrweck, *Z. Phys.*, 1977, **A280**, 17–25; 125–130; U. Hauser, V. Oestreich and H. D. Rohrweck, *Z. Phys.*, 1978, **A284**, 9–19.
17 M. D. Carducci, M. R. Pressprich and P. Coppens, *J. Am. Chem. Soc.*, 1997, **119**, 2669–2678.
18 P. Coppens, I. Novozhilova and A. Kovalevsky, *Chem. Rev.*, 2002, **102**, 861–883.
19 M. Kawano, A. Ishikawa, Y. Morioka, H. Tomizawa, E. Miki and Y. Ohashi, *J. Chem. Soc., Dalton Trans.*, 2000, 2425–2431.
20 C. Kim, I. Novozhilova, M. S. Goodman, K. A. Bagley and P. Coppens, *Inorg. Chem.*, 2000, **39**, 5791–5795.
21 S. Ferlay, H. W. Schmalle, G. Francese, H. Stoeckli-Evans, M. Imlau, D. Schaniel and T. Woike, *Inorg. Chem.*, 2004, **43**, 3500–3506.
22 D. Schaniel, T. Woike, C. Boskovic and H.-U. Güdel, *Chem. Phys. Lett.*, 2004, **390**, 347–351.
23 D. Schaniel, T. Woike, B. Delley, C. Boskovic, D. Biner, K. W. Krämer and H.-U. Güdel, *Phys. Chem. Chem. Phys.*, 2005, **7**, 1164–1170.
24 J. H. Enemark and R. D. Feltham, *Coord. Chem. Rev.*, 1974, **13**, 339–406.
25 D. Schaniel, M. Imlau, T. Weisemoeller, T. Woike, K. W. Krämer and H.-U. Güdel, *Adv. Mater.*, 2007, **19**, 723–726.
26 T. Woike, B. Haussühl, B. Sugg, R. A. Rupp, J. Beckers, M. Imlau and R. Schieder, *Appl. Phys. B: Lasers Opt.*, 1996, **63**, 243–248.
27 T. Woike, M. Imlau, S. Haussühl, R. A. Rupp and R. Schieder, *Phys. Rev. B: Condens. Matter Mater. Phys.*, 1998, **58**, 8411–8415.
28 M. Imlau, T. Woike, R. Schieder and R. A. Rupp, *Phys. Rev. Lett.*, 1999, **82**, 2860–2863.
29 T. Woike, H. Zöllner, W. Krasser and S. Haussühl, *Solid State Commun.*, 1990, **73**, 149–152.
30 T. Woike, unpublished results.
31 D. Schaniel, unpublished results.
32 D. Schaniel, B. Cormary, I. Malfant, L. Valade, T. Woike, B. Delley, K. W. Krämer and H.-U. Güdel, *Phys. Chem. Chem. Phys.*, 2007, **9**, 3717–3724.
33 L. G. F. Lopes, A. Wieraszko, Y. El-Sherif and M. J. Clarke, *Inorg. Chim. Acta*, 2001, **312**, 15–22.
34 K. Ookubo, Y. Morioka, H. Tomizawa and E. Miki, *J. Mol. Struct.*, 1996, **379**, 241–247.
35 J. M. Slocik, M. S. Ward, K. V. Somayajula and R. E. Shepherd, *Transition Met. Chem.*, 2001, **26**, 351–364.
36 I. A. Efimenko, A. P. Kurbakova, T. A. Balakaeva, V. E. Mistryukov, Yu. N. Mikhailov and A. S. Kanishcheva, *Zh. Neorg. Khim.*, 1991, **36**, 1765–1771.
37 S. da S. S. Borges, C. U. Davanzo, E. E. Castellano, J. Z-Schpector, S. C. Silva and D. W. Franco, *Inorg. Chem.*, 1998, **37**, 2670–2677.
38 T. A. Balakaeva, A. V. Churakov, M. G. Ezernitskaya, L. G. Kuz'mina, B. V. Lokshin and I. A. Efimenko, *Russ. J. Coord. Chem.*, 1999, **25**, 579–583.
39 D. Cremer and J. A. Pople, *J. Am. Chem. Soc.*, 1975, **97**, 1354–1358.
40 W. S. Sheldrick and R. Exner, *Inorg. Chim. Acta*, 1992, **195**, 1–9.
41 A. P. Scott and L. Radom, *J. Phys. Chem.*, 1996, **100**, 16502–16513.
42 H. Zöllner, T. Woike, W. Krasser and S. Haussühl, *Z. Kristallogr.*, 1989, **188**, 139–153.
43 J. A. Guida, O. E. Piro and P. J. Aymonino, *Inorg. Chem.*, 1995, **34**, 4113–4116.
44 J. R. Durig, W. A. McAllister, J. N. Willis, Jr. and E. E. Mercer, *Spectrochim. Acta*, 1966, **22**, 1091–1100.
45 M. J. Frisch, G. W. Trucks, H. B. Schlegel, G. E. Scuseria, M. A. Robb, J. R. Cheeseman, J. A. Montgomery, Jr., T. Vreven, K. N. Kudin, J. C. Burant, J. M. Millam, S. S. Iyengar, J. Tomasi, V. Barone, B. Mennucci, M. Cossi, G. Scalmani, N. Rega, G. A. Petersson, H. Nakatsuji, M. Hada, M. Ehara, K. Toyota, R. Fukuda, J. Hasegawa, M. Ishida, T. Nakajima, Y. Honda, O. Kitao, H. Nakai, M. Klene, X. Li, J. E. Knox, H. P. Hratchian, J. B. Cross, V. Bakken, C. Adamo, J. Jaramillo, R. Gomperts, R. E. Stratmann, O. Yazyev, A. J. Austin, R. Cammi, C. Pomelli, J. W. Ochterski, P. Y. Ayala, K. Morokuma, G. A. Voth, P. Salvador, J. J. Dannenberg, V. G. Zakrzewski, S. Dapprich, A. D. Daniels, M. C. Strain, O. Farkas, D. K. Malick, A. D. Rabuck, K. Raghavachari, J. B. Foresman, J. V. Ortiz, Q. Cui, A. G. Baboul, S. Clifford, J. Cioslowski, B. B. Stefanov, G. Liu, A. Liashenko, P. Piskorz, I. Komaromi, R. L. Martin, D. J. Fox, T. Keith, M. A. Al-Laham, C. Y. Peng, A. Nanayakkara, M. Challacombe, P. M. W. Gill, B. Johnson, W. Chen, M.W. Wong, C. Gonzalez, J. A. Pople, *Gaussian 03*, Revision C.02, Gaussian, Inc., Wallingford, CT, 2004.
46 D. Andrae, U. Häußermann, M. Dolg, H. Stoll and H. Preuß, *Theor. Chim. Acta*, 1990, **77**, 123–141.
47 T. H. Dunning, P. J. Hay, in *Modern Theoretical Chemistry*, ed. H. F. Schaefer, Plenum, New York, 3rd edn, 1976, vol. 3, pp. 1–28.
48 C. Lee, W. Yang and R. G. Parr, *Phys. Rev. B: Condens. Matter Mater. Phys.*, 1988, **37**, 785–789.
49 S. H. Vosko, L. Wilk and M. Nusair, *Can. J. Phys.*, 1980, **58**, 1200–1211.
50 P. J. Stephens, F. J. Devlin, C. F. Chabalowski and M. J. Frisch, *J. Phys. Chem.*, 1994, **98**, 11623–11627.
51 A. D. Becke, *J. Chem. Phys.*, 1993, **98**, 5648–5652.
52 B. Miehlich, A. Savin, H. Stoll and H. Preuss, *Chem. Phys. Lett.*, 1989, **157**, 200–206.
53 T. H. Dunning, Jr., *J. Chem. Phys.*, 1989, **90**, 1007–1023.
54 W. J. Hehre, L. Random, P. v. R. Schleyer and J. A. Pople, *Ab Initio Molecular Orbital Theory*, Wiley, New York, 1986.
55 J. P. Perdew, K. Burke and M. Ernzerhof, *Phys. Rev. Lett.*, 1996, **77**, 3865–3868.
56 J. P. Perdew, K. Burke and M. Ernzerhof, *Phys. Rev. Lett.*, 1997, **78**, 1396.